

# Dynamic Waveform Shaping With Picosecond Time Widths

Xue Wu, *Student Member, IEEE*, and Kaushik Sengupta, *Member, IEEE*

**Abstract**—In this paper, we present a scalable architecture in silicon that allows synthesis and dynamic waveform shaping of periodic mm-wave signals, either generated on-chip or quasi-optically through radiation in free space capable of producing pulse trains with picosecond time signatures. This is achieved through an architecture that allows extraction of multiple harmonics above  $f_{\max}$  with simultaneous amplitude and phase control. Signal synthesis is achieved through controlled interference of multiple traveling waves with rich harmonic components and delays. The first example, presented in this paper, is where the signal synthesis is achieved on-chip demonstrating a pulse train at the output with a measured pulsedwidth of 2.6 ps and a 0.46-mW output power. The second example is a four-element array with integrated antennas, which allows signal synthesis in space and is demonstrated to show reconfigurable radiation of pulse trains with a 2.6-ps pulsedwidth, pure tones at a fundamental frequency of 107.5 GHz with an effective isotropic radiated power (EIRP) of 4.6 dBm and a second harmonic of 215 GHz with EIRP of 5.0 dBm, as well as any combination of these two harmonics with arbitrary amplitudes and delays. To the best of the authors' knowledge, this paper demonstrates the sharpest on-chip and radiated pulses with dynamic waveform shaping in any integrated circuit technology. This can open the door to innovations in broadband terahertz imaging, sensing, and spectroscopy.

**Index Terms**—Antennas, arrays, beam-forming, CMOS, mm-wave, picosecond, signal generation, terahertz, waveform shaping.

## I. INTRODUCTION

TIME signatures with picosecond time widths have rich applications ranging from high-resolution radar and imaging to spectroscopic sensing in chemical and biomedical sciences due to large molecules having vibrational and rotational information in the terahertz frequency range. Classically, such wideband terahertz signals are generated and detected by exploiting picosecond dynamics of free carriers when femtosecond lasers impinge on photoconductive substrates [1]–[4]. While terahertz technology has traditionally been realized with III–V-based compound semiconductors or optics-based systems, in recent years, silicon-based integrated systems have been demonstrated to operate near and above

Manuscript received March 10, 2016; revised June 21, 2016 and July 29, 2016; accepted October 4, 2016. Date of publication December 14, 2016; date of current version January 30, 2017. This paper was approved by Associate Editor Kenichi Okada.

The authors are with the Integrated Micro-systems Research Laboratory, Department of Electrical Engineering, Princeton University, Princeton, NJ 08544 USA (e-mail: xuew@princeton.edu).

Color versions of one or more of the figures in this paper are available online at <http://ieeexplore.ieee.org>.

Digital Object Identifier 10.1109/JSSC.2016.2616349

300 GHz, capable of generating output power in the milliwatt range [5]–[26]. There are still tremendous challenges in enabling efficient power generation and detection at these frequencies using silicon-based IC technology particularly due to low carrier mobility, limited cutoff frequency  $f_{\max}$ , low-quality passives in silicon, and lower gate breakdown voltages. Therefore, generally, continuous-wave power generation above  $f_{\max}$  has been accomplished through harmonic power generation by exploiting nonlinearities inherent in the active devices and the undesired harmonics have been filtered using circuit architectures that inherently suppress the fundamental and other undesirable harmonics [8]–[21]. Examples of such architectures can be seen in the early works of radiating terahertz CMOS oscillators where the second and fourth harmonics were extracted out of the common mode nodes generating signals at 410 and 553 GHz with 20 and 220 nW of the output power, respectively [8], [9]. Similarly, in [10] and [11], the fundamental frequency signal was quasi-optically suppressed and the second harmonic selectively radiated through a distributed active radiator architecture. In [17], design methodologies were proposed to realize the optimal oscillator topology that extracts the desirable harmonic with highest efficiency, while suppressing the others. In a similar fashion, the following works in [18]–[27] demonstrate various integrated architectures capable of generating and extracting pure tone signals in the mm-wave and terahertz frequency range. In this paper, we present a scalable architecture that harnesses multiple harmonics beyond  $f_{\max}$  with individual amplitude and phase control, which can be programmed to enable reconfigurable periodic signal synthesis and waveform shaping either on-chip or quasi-optically in free-space.

The motivation for this paper stems from the fact that a train of picosecond pulses of width ( $\Delta t \sim 1$  ps) at a pulse repetition frequency of  $f_{\text{rep}}$  contains harmonics of  $f_{\text{rep}}$ . The spectral envelope follows the spectrum of the pulse shape and the phase is ideally linear with constant group delay extending up to the highest harmonic  $Mf_{\text{rep}}$  in the terahertz frequency range ( $Mf_{\text{rep}} \sim 1/\Delta t \approx 1$  THz), as shown in Fig. 1. It is analogous to a mode-locked optical laser where the multiple harmonics align up in phase resulting in femtosecond pulses emanating from the output. Therefore, the key toward the generation of picosecond pulses is to harness multiple harmonics above  $f_{\max}$  with simultaneous amplitude and phase controls, such that all the components have equal amplitudes and proportional phases. When these harmonics align up in this fashion, sharp pulses are generated with time widths [full-width at half-maximum (FWHM)]  $\Delta t \sim 1/(2nf_0)$ . This is

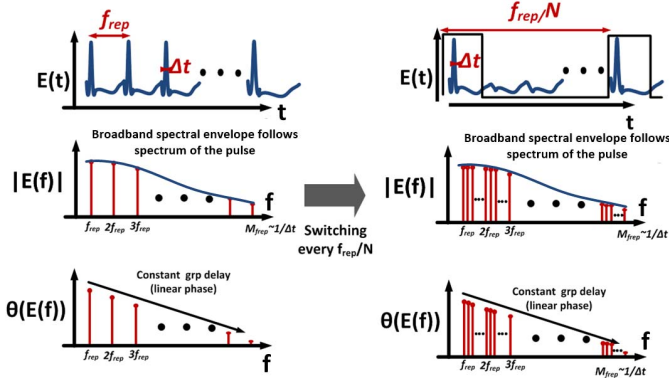


Fig. 1. Train of picosecond pulses at  $f_{rep}$  consisting of harmonics of  $f_{rep}$  with linear phase progression or constant group delay. Once the periodic time signatures are generated, the repetition frequency can be modulated by switching off the signal periodically to shape the frequency spectrum.

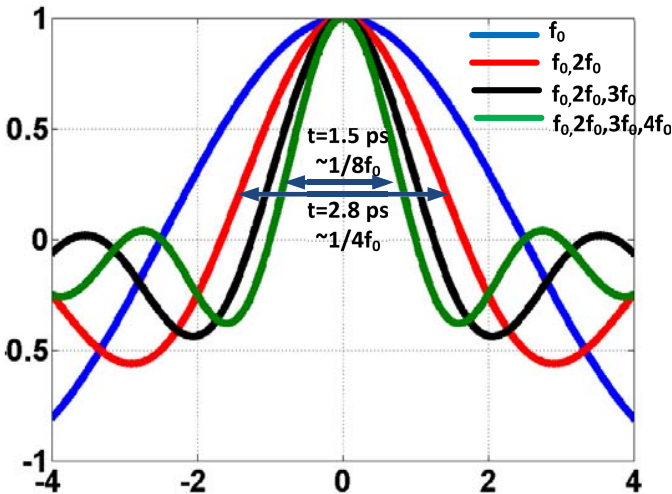


Fig. 2. Sharpening the pulse train with the addition of more harmonics approaching an impulse in the limit. Time width is defined as FWHM.

illustrated in Fig. 2, which shows the sharpening of the pulse as more harmonics are added to a fundamental frequency of 100 GHz. In the limit, with infinite harmonics, the signal will converge to an impulse. Additionally, being able to control the amplitudes and phases of all the harmonics allows us to dynamically shape the radiated field spectrum in addition to being able to overcome dispersion losses in the radiation path. This degree of reconfigurability is critically important at these frequencies where dispersion due to on-chip antenna, lossy substrates and effects of process variations, and mismatches and modeling inaccuracies becomes critically important and can affect other demonstrated methods of broadband signal generation [29]–[35]. As shown in Fig. 1, once the periodic time signatures are generated, the repetition frequency can be modulated by switching off the signal periodically at a lower frequency. The proposed method can significantly relax the requirement of the switching speed. As Fig. 1 illustrates, to generate a pulse with a pulselwidth of the order of  $\Delta t \sim 1/(2nf_0)$ , a switch-based pulse generation architecture will need to operate with duty cycles of the same time order of

$\Delta t \sim 1/(2nf_0)$ . Understandably, for picosecond pulses, realizing such high-speed switches with transistors with limited  $f_{max}$  is extremely challenging. In addition, the switch performance trades off directly with output power because of parasitic scaling, which also makes it susceptible to nonidealities such as process variations, modeling inaccuracies, dispersion, and mismatches. Post-fabrication reconfigurability for alignment of amplitudes and phases to overcome these challenges becomes critical. The proposed architecture addresses both of these issues simultaneously. It can relax the switching time window to  $1/f_0$  as shown in Fig. 1 by achieving the waveform shaping with multiple harmonics above  $f_{max}$ . In addition, phase and amplitude programmability helps us to overcome nonidealities as well as achieve dynamic waveform shaping capable of generating time signatures with picosecond time widths.

In order to demonstrate the validity of the approach, we present two architectures.

- 1) A programmable on-chip pulse generator that harnesses two harmonics at 107 and 214 GHz with precise amplitude and delay control to generate a picosecond pulse train with a pulselwidth of 2.6 ps and 0.46-mW output power.
- 2) A  $4 \times 1$  array with on-chip antennas generating and radiating multi-harmonic signals with the capability of dynamic waveform shaping in free space. The chip is demonstrated to radiate in a reconfigurable fashion, producing pulse trains with 2.6-ps time widths, pure tones at a fundamental frequency of 107.5 GHz, and a second harmonic of 215 GHz with EIRPs of 4.6 and 5 dBm, respectively, and any combination of the two harmonics with programmable amplitudes and delays.

The chips are implemented in a 65-nm low power (LP)-CMOS process with  $f_{max} \sim 190$  GHz. The rest of this paper is organized as follows. Section II explains the conceptual architecture for both on-chip and the radiating array architecture for reconfigurable waveform shaping. Section III describes the constituent circuit blocks and implementation details. In Section IV, custom measurement setups for measuring amplitude and phase in frequency domain are illustrated and the detailed measurement results are presented.

## II. OVERVIEW OF THE ARCHITECTURE

Fig. 3 shows a conceptual architecture capable of shaping the time evolution of the generated signal by harnessing multiple harmonic frequencies beyond  $f_{max}$  through an array of locked sources. With amplitude and phase control, any pure tone from  $f_0$  to  $nf_0$  and any combination of them can be routed to the output in a programmable fashion. As an example shown in Fig. 3, if the amplitudes of all the harmonics are the same, but the phases are randomly assigned, then the energy of the synthesized signal will be uniformly distributed over time. However, by rotating the phase shifters, if the harmonic signals are allowed to align up in time, then bursts of energy in the form of a pulse train are generated at the output. This happens because the maxima of all the harmonic frequencies align up

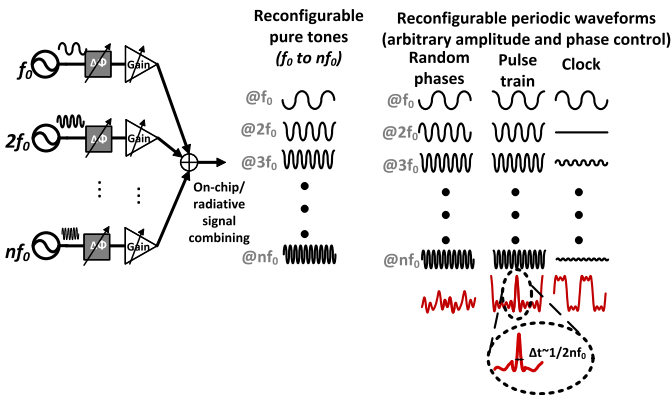


Fig. 3. Conceptual architecture capable of shaping the time evolution of the generated signal by harnessing multiple harmonic frequencies beyond  $f_{\max}$  through an array of locked sources.

for a short time interval, and they almost cancel each other at all other times. Due to this effect, the pulsedwidths of the synthesized pulse train are around half of the time period of the highest harmonic ( $\Delta t \sim 1/(2nf_0)$ ). Therefore, if multiple harmonics are extracted with amplitude and phased control such that  $nf_0 \sim nf_{\max}$ , then pulsedwidths of the order of  $1/(2nf_{\max})$  can be generated at the output. As an example, for a 65-nm bulk CMOS process with  $f_{\max}$  of 190 GHz, pulsedwidths of the order of 1.31 ps can be generated with harmonic control up to 380 GHz. In addition, with amplitude and phase control of each harmonic, dynamic waveform shaping can be achieved at the output. As an example, when the odd harmonics are in phase and their amplitudes are inversely proportional to their frequencies, and the even harmonics are eliminated, an ultrafast clock waveform can be generated with picosecond rise and fall times. Signal combination can be achieved on-chip or in free space by allowing quasi-optical combination of the individual waveforms. In this paper, we will demonstrate examples of both of these signal combining methodologies.

A straightforward architecture to generate these multiple frequencies, filter, isolate, and combine them with amplitude and phase control is shown in Fig. 4(a). Signals from a source at  $f_0$  ( $< f_{\max}$ ) are centrally distributed to multiple channels with nonlinear devices to generate a series of harmonic frequencies beyond  $f_{\max}$ . In order to extract different harmonic frequencies across different channels, the signals undergo on-chip bandpass filtering and are then combined with amplitude and phase control.<sup>1</sup> Evidently, this is not the most efficient method for realization of the architecture. First, passive filtering of the individual signals at such high harmonic frequencies can be very inefficient due to the limited quality factor of integrated passives and variability of the precise tuning frequency due to process variations and mismatches. Second, since no power amplification is possible beyond  $f_{\max}$ , gain control can only be implemented with variable attenuation.

<sup>1</sup>Conceptually, it is also possible to directly implement each channel with a different set of locked harmonic oscillators capable of extracting pure tones at different harmonic frequencies such as those demonstrated with fourth [9], second [10], [11], third [21], or even higher ones [27].

In addition, active and passive phase shifting at harmonic frequencies beyond  $f_{\max}$  will also lead to significant losses reducing output power and efficiency.

In order to overcome these challenges, the architecture is modified into the one in Fig. 4(b), which eliminates the need for separate harmonic filtering, gain control, and phase control at higher harmonic frequencies and simultaneously achieves all of them by establishing phase control at the lower fundamental frequency  $f_0$ . As will be shown later, this is achieved by carefully combining controllable delayed versions of multiple harmonically rich signals through the various paths in such a fashion that the amplitudes and phases of all the combining harmonics can be controlled separately. It can be noted that the phase rotators only operate at the lowest frequency  $f_0$  and therefore can be a narrowband and efficient. Further, unlike the methodology shown in Fig. 4(a), the proposed architecture is fully symmetrical with identical branches enabling a modular and scalable design. In addition, the ability to reconfigure the waveform with the phase control settings at  $f_0$  allows the architecture to be able to spectrally shape the radiated waveforms and also to be robust to process variations and dispersion in output combining, either on-chip or quasi-optically through integrated antennas.

By subsuming the amplitude, phase controls, and harmonic filtering into the phase rotator settings at  $f_0$ , the number of paths has to be carefully chosen to enable the proposed reconfigurability with the desired number of harmonics. Fig. 5 presents an example of such reconfigurable waveform synthesis. Four nonlinear channels generate harmonic frequencies ( $f_0 - 4f_0$ ) with different amplitudes and aligned in phase as shown by the vector representation. If the fundamental frequency signal driving the channels is rotated by  $90^\circ$  in progression, the phases of the higher harmonics in each channel are also proportionately rotated, as illustrated in Fig. 5. If the signals are combined together, all the harmonics except the fourth are canceled, resulting in an architecture that extracts a pure tone at the fourth harmonic. Evidently, by changing the phase rotator settings, different waveforms can be synthesized through interference of the different harmonics at the output. However, it can also be argued that the four-path architecture for four harmonics allows only a subset of possible combinations of the signals. As an example, the architecture cannot be programmed to extract only the second harmonic. If the fundamental signal at  $f_0$  is rotated by  $180^\circ$ , in addition to the second, the fourth harmonic will also combine in phase. Therefore, independent control for amplitudes and phases of ' $n$ ' harmonics cannot be achieved with ' $n$ ' channels. The analysis for minimum number of channels to control ' $n$ ' harmonics will be carried out with the architecture for on-chip combining, but is equally applicable for radiated free-space combining.

Fig. 6 demonstrates the on-chip combining topology that achieves the signal combination with delay control in a broadband multiport transmission line. The proposed architecture exploits device nonlinearities to produce a series of harmonic frequencies and employs controllable interference of traveling waves to generate arbitrary amplitudes and phases of the spec-

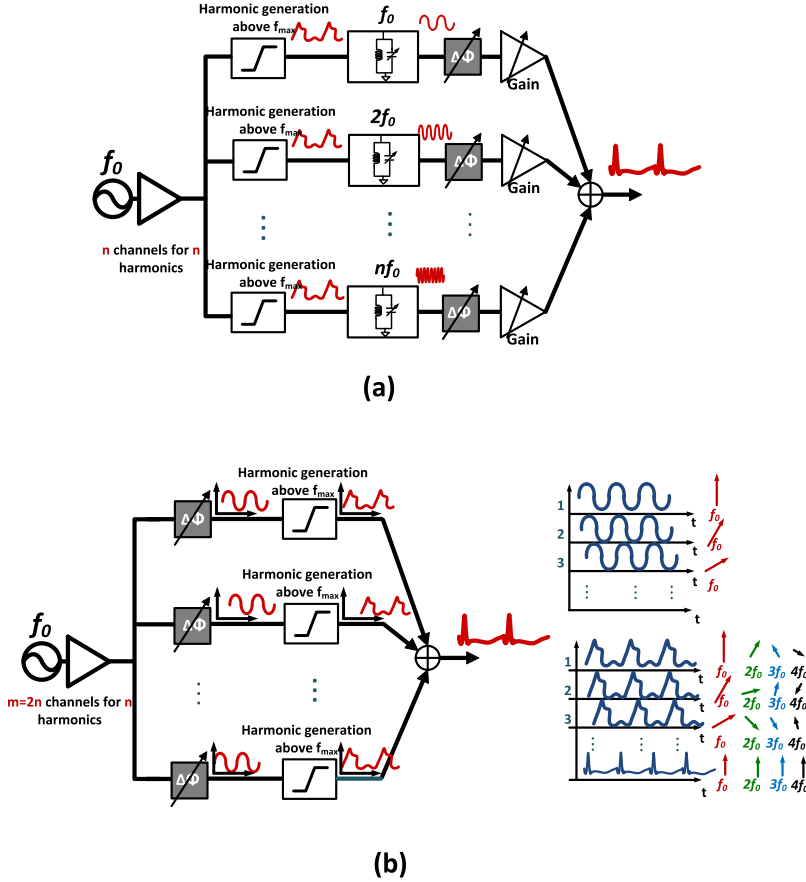


Fig. 4. (a) Conceptual architecture for dynamic waveform shaping exploiting nonlinearities of the transistors for harmonic generation. (b) Proposed scalable architecture for reconfigurable multi-harmonic signal generation with arbitrary amplitude and phase. The architecture eliminates the need for lossy passive filtering, gain control for frequencies near and above  $f_{max}$ , and lossy higher harmonic frequency phase shifters and achieves the same through phase control of the fundamental signal. Signal synthesis is achieved by a linear combination of the different delayed harmonic signals on-chip or through quasi-optical free-space combining.

tral components. A central frequency synthesizer operating at  $f_0$  below  $f_{max}$  distributes the fundamental signal into multiple (' $m$ ') channels. In each channel, a narrowband phase rotator working at  $f_0$  controls the phase of the fundamental signal, which drives a nonlinear block that launches a traveling wave with rich harmonic frequencies into the  $t$ -line-based multiport interference medium for combining, as shown in Fig. 6. A rotation of  $\Delta\theta$  at  $f_0$  creates proportional phase changes for the higher harmonics in each channel. If  $(A_i, \theta_i)$  represent the amplitude and phase of the  $i$ th harmonic for the desirable waveform at the output, and the constituent harmonic components of the nonlinear block (harmonic generator) output are represented by the Volterra series,  $(i_{f_0}, i_{2f_0}, i_{3f_0} \dots, i_{nf_0}) = (a_1 e^{j\phi_1}, a_2 e^{j\phi_2}, a_3 e^{j\phi_3}, \dots, a_n e^{j\phi_n})$ , then the harmonic components of the combined output of ' $m$ ' channels can be represented as

$$\begin{aligned} A_1 e^{j\theta_1} &= a_1 e^{j\phi_1} (e^{j(\Delta\theta_1 + \psi_1)} + \dots e^{j(\Delta\theta_m + m\psi_1)}) \\ A_2 e^{j\theta_2} &= a_2 e^{j\phi_2} (e^{j(2\Delta\theta_1 + \psi_2)} + \dots e^{j(2\Delta\theta_m + m\psi_2)}) \\ &\dots \\ A_n e^{j\theta_n} &= a_n e^{j\phi_n} (e^{j(n\Delta\theta_1 + \psi_n)} + \dots e^{j(n\Delta\theta_m + m\psi_n)}) \end{aligned} \quad (1)$$

where  $\psi_k$  represents the phase shift suffered by the  $k$ th harmonic when it travels through one section of the  $t$ -line and combines at the output. If the  $t$ -line is dispersionless,  $\psi_k = k\psi_1$ . For  $n$  harmonics, amplitude and phase control implies  $2n$  equations where the number of variables are the number of phase shifters in the  $m$  channels. Therefore,  $m = 2n$  denotes the minimum number of channels for which arbitrary control for all the harmonics can be achieved with simple phase control at the fundamental frequency. By eliminating the need for passive filtering, high-frequency phase shifters, and amplitude control, the number of paths is increased by a factor of two. However, the architecture is scalable and provides the flexibility to choose how the phase rotations are distributed through  $\Delta\theta_i$  and the delay line  $\psi_i$ . Even for a  $t$ -line with dispersion, since  $a_i$  and  $\psi_i$  are constants, it is possible to arrive at a solution for  $(\Delta\theta_i)$  for any desirable  $(A_i, \theta_i)$  when the number of channels provides enough degree of freedom to reconfigure all the harmonics. Of course, a nonlinear solver needs to be employed to evaluate the phase rotator settings. As an example, suppose for three harmonic components, we have the following:  $(a_1 e^{j\phi_1}, a_2 e^{j\phi_2}, a_3 e^{j\phi_3}) = (1, 0.3 e^{i\pi/4}, 0.1 e^{i\pi/3})$  [Fig. 7(a)]. Then, from (1), as shown in Fig. 7(b) and (c), the phase rotator settings can be evaluated for four different

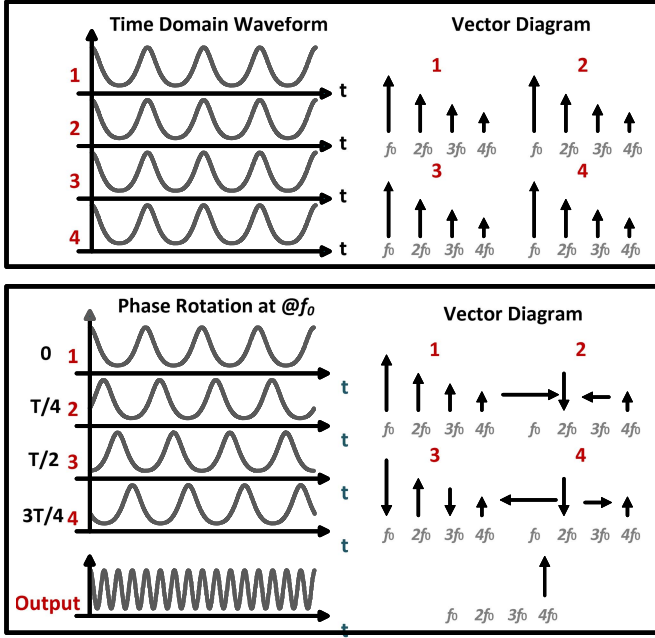


Fig. 5. Examples of waveform reconfiguration with phase control at fundamental frequency  $f_0$ .

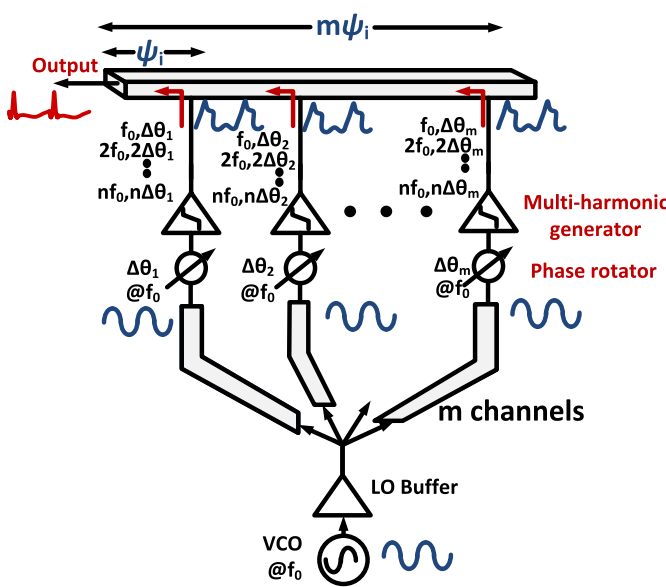


Fig. 6. Proof-of-concept architecture for programmable on-chip mm-wave periodic waveform synthesis where dynamic waveform shaping is achieved through interference of multiple traveling waves with different delays in the multiport transmission medium.

output waveform configurations including pure tones at each frequency and a pulse train with equal amplitude and proportional phases (nearly zero in this case).

Signal combining can also be achieved in space by radiating the harmonically rich signals in each channel with integrated antennas and the desirable waveform is synthesized in space in a given direction due to the superposition in the far field of the individual electromagnetic fields of the constituent harmonics. The proof of concept architecture is shown in Fig. 8. Similar

to the previous architecture, the fundamental signal at  $f_0$  below  $f_{\max}$  is distributed into multiple channels from a central frequency synthesizer. Each nonlinear channel generates a series of harmonic frequencies that are radiated by individual antennas. The signal synthesis through the radiative combination of multiple harmonic-rich signals happen at the far field in the intended direction. However, unlike an on-chip transmission line combining, integrated antennas can excite multiple frequency-dependent substrate waves, which can distort the radiation patterns and induce dispersion on the radiated spectral components. The ability to control the amplitude and phases of the individual spectral components through the phase rotator settings also allows us to overcome these effects in addition to enabling reconfiguration of the waveforms. If  $(E_i, \theta_i)$  denotes the amplitude and phase of the field for the  $i$ th harmonic for the desirable signal in free space in an intended angle  $\beta$  from the antenna plane, and the radiated signal from each channel has the following constituent harmonics:  $E_{f0}, E_{2f0}, E_{3f0} \dots, E_{nf0} = \alpha_1 e^{j\phi_1}, \alpha_2 e^{j\phi_2}, \dots, \alpha_n e^{j\phi_n}$  for  $\Delta\theta_1 = 0$ , then the combined signal of ' $m$ ' channels has the following spectral relationship:

$$\begin{aligned} E_1 e^{j\theta_1} &= \alpha e^{j\phi_1} \left( e^{j\Delta\theta_1} + \dots e^{j\Delta\theta_m + \frac{2\pi(m-1)d}{\lambda_{f0}} \cos(\beta)} \right) \\ E_2 e^{j\theta_2} &= \alpha e^{j\phi_2} \left( e^{j2\Delta\theta_1} + \dots e^{j2\Delta\theta_m + \frac{4\pi(m-1)d}{\lambda_{f0}} \cos(\beta)} \right) \\ &\dots \\ E_n e^{j\theta_n} &= \alpha e^{j\phi_n} \left( e^{jn\Delta\theta_1} + \dots e^{jn\Delta\theta_m + \frac{2n\pi(m-1)d}{\lambda_{f0}} \cos(\beta)} \right) \end{aligned} \quad (2)$$

where  $\lambda_{f0}$  is the wavelength of the fundamental frequency in free space. It can be seen from (2) that similar to on-chip combining, the minimum number of channels for any desirable  $(E_i, \theta_i)$  is given by  $m = 2n$ . In the implemented architecture, phase control of the driving signal at  $f_0$  not only allows us to dynamically reconfigure the waveform in free space and overcome dispersion, but also in theory allows electronic beam-steering of the radiated time signatures. In the presence of dispersion and process variations, the amplitude and phase distortions can be included in the terms  $\alpha_1 e^{j\phi_1}, \alpha_2 e^{j\phi_2}, \alpha_3 e^{j\phi_3}, \dots, \alpha_n e^{j\phi_n}$  and a new set of phase conditions can be derived and programmed for the desired pulse shape. This allows robustness in the presence of nonidealities, which is critical at these frequencies.

### III. CONSTITUENT CIRCUIT BLOCKS AND IMPLEMENTATION DETAILS

In order to demonstrate the concept, a programmable picosecond on-chip pulse generator and a  $4 \times 1$  array for reconfigurable signal synthesis in free space are implemented. In the implementation, we consider architectures that exploit two harmonic frequencies to demonstrate the concept of waveform shaping. However, the architectures can certainly be modified to take higher harmonics into consideration by allowing more signal paths to combine.

#### A. On-Chip Picosecond Pulse Generator

An architecture for on-chip signal combining optimized for picosecond time-signatures is shown in Fig. 9.

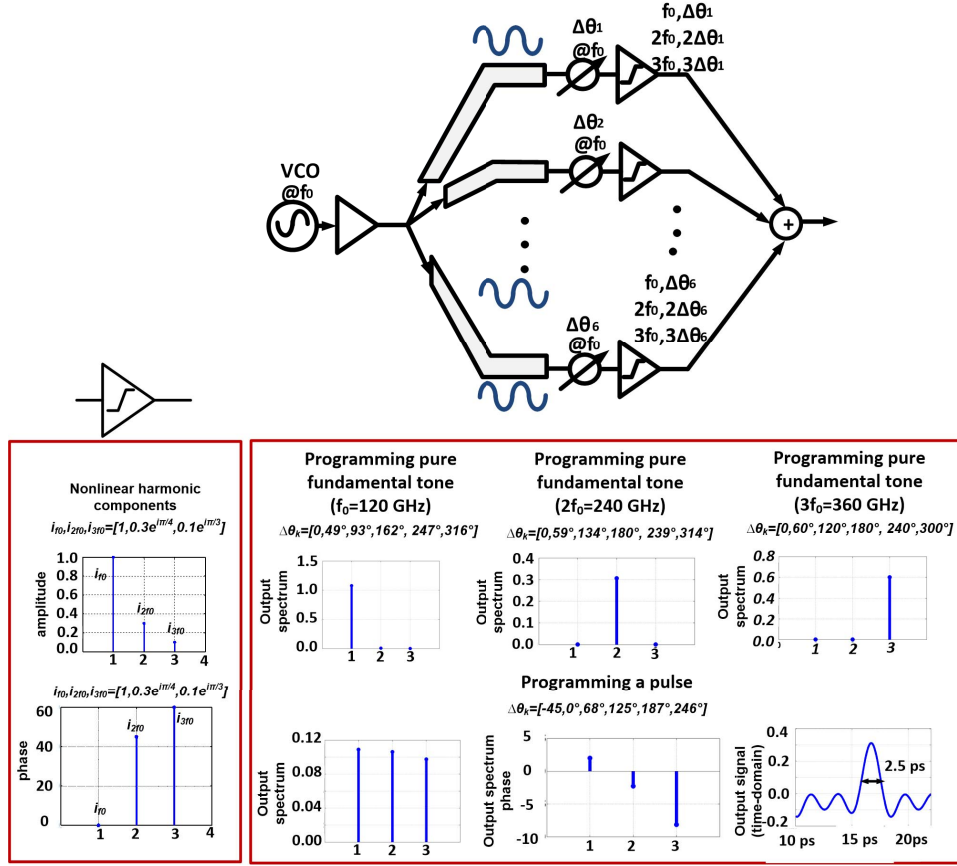


Fig. 7. Example solution for the phase settings in six channels for signal synthesis with three harmonics. The solution shows the phase settings for four examples including pure tones at each frequency and a pulse train. (a) Example of harmonic components generated by the nonlinear block. (b) Phase settings for pure tone signal generations at different harmonics. (c) Phase settings for a pulse train generation and simulated spectrum (magnitude and phase) and time-domain waveforms of the resultant pulse train.

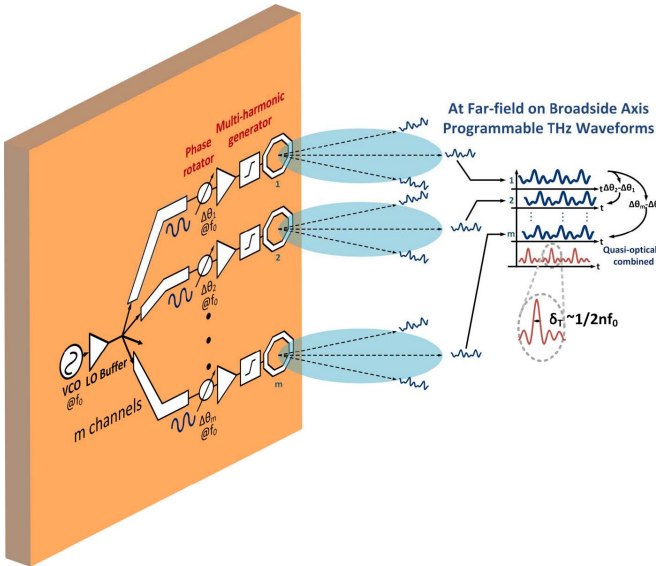


Fig. 8. Array architecture with on-chip antennas for reconfigurable radiated signal synthesis where dynamic waveform shaping is achieved through quasi-optically combining multiple harmonic rich electromagnetic waves with different delays.

The architecture exploits two harmonics and allows them to combine on a two-port  $t$ -line with equal amplitude and a phase offset ( $2\theta_{f0} - \theta_{2f0}$ ) of  $180^\circ$  to generate an output of inverted

pulse train. A voltage-controlled oscillator (VCO) is locked to a reference and provides a differential signal at 108 GHz ( $f_0$ ). The fundamental signal is buffered and amplified by two cascaded amplifiers with  $t$ -line-based matching networks to generate sufficient power for efficient harmonic generation. The amplified signal passes through variable delay lines and drives two pseudo-differential transistors, which are biased optimally for strong nonlinear harmonic generation. The outputs of the harmonic generators are combined in a two-port  $t$ -line medium for pulse generation, as shown in Fig. 9.

In order to align the harmonics for pulse generation, the phases of the fundamental frequency at 108 GHz and the second harmonic signal at 216 GHz should satisfy  $2\theta_{f0} = \theta_{2f0}$  or  $2\theta_{f0} = \theta_{2f0} + \pi$ . As shown in Fig. 10, the second condition can be satisfied if interference is allowed on a suitable transmission line of length, such that the harmonic current vectors rotate and align in the required amplitude and phase relations. It can be shown that if  $i_{f0}$  and  $i_{2f0}$  are the amplitudes of the harmonic currents and if the  $t$ -line is terminated in a matched impedance, then the required length of the transmission line is given by the following relation:  $i_{f0} \sin(\psi_{f0}/2) = i_{2f0} \cos(\psi_{2f0}/2)$ . However, the symmetry of the architecture allows for analysis of the waveform shaping by observing the phase rotations of the voltage waveforms due to the different impedances seen by the

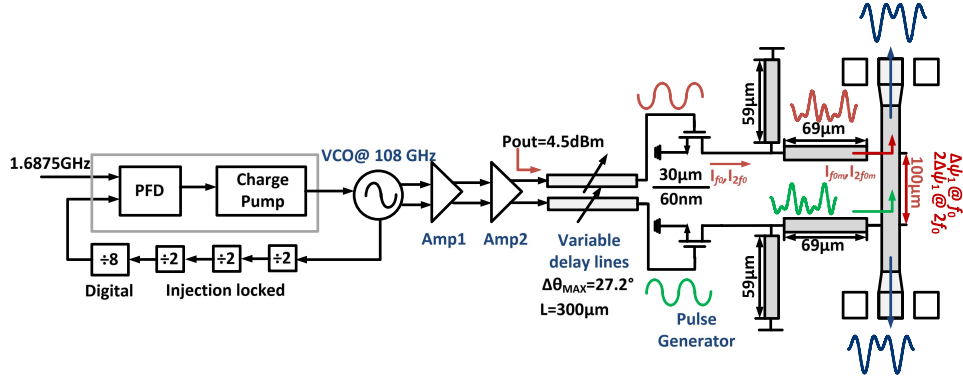


Fig. 9. Programmable picosecond on-chip pulse generator, which exploits two harmonic frequencies at 108 and 216 GHz to align them with a phase offset of 180° at the two outputs to generate pulses of 2.6-ps time widths.

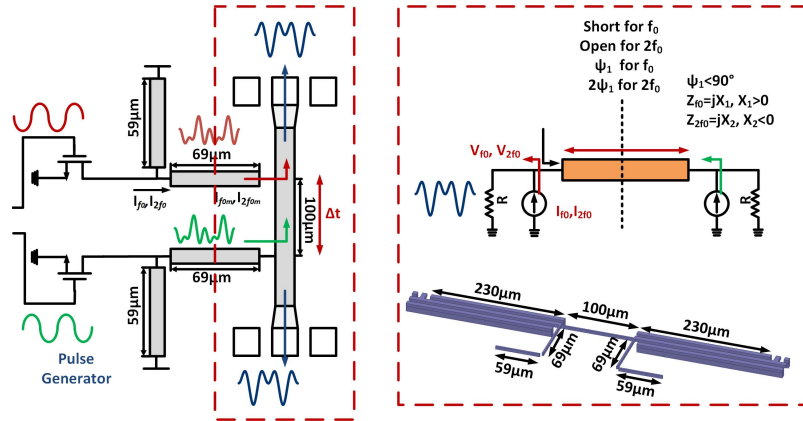


Fig. 10. Schematic and analysis of the pulse generator.

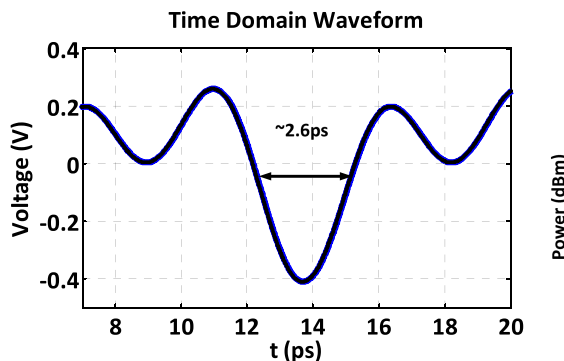


Fig. 11. Time-domain waveform of the generated pulse train.

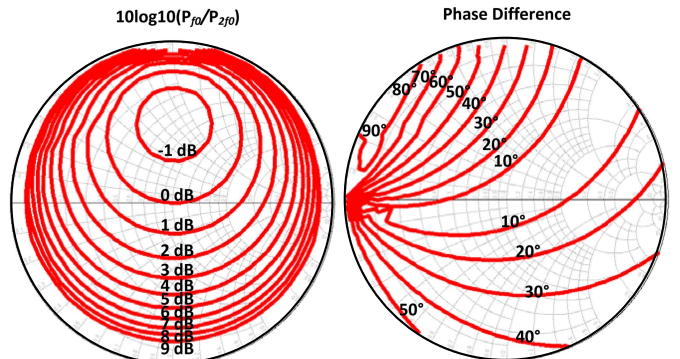


Fig. 12. Variations of power difference and phase offset between the two harmonics with variation in the output impedance.

nonlinear active devices at the different harmonic frequencies. The transistors are modeled as ideal current sources with two harmonics with differential operation at  $f_0$  (108 GHz) and in-phase operation at  $2f_0$  (216 GHz), as shown in Fig. 10. Due to the differential- and common-mode operation at the two harmonics, the half-circuit model of the architecture presents purely imaginary impedances  $jX_{f0} = jZ_0 \tan(\beta_{f0}l/2)$  and  $jX_{2f0} = -jZ_0 \cot(\beta_{2f0}l/2)$  to the two harmonics. The harmonic components of the generated output voltage can

be expressed as follows:

$$V_{f0} = \frac{jX_{f0}I_{f0}}{R + jX_{f0}}R \quad (3)$$

$$V_{2f0} = \frac{jX_{2f0}I_{2f0}}{R + jX_{2f0}}R \quad (4)$$

where  $V_{f0}$  and  $V_{2f0}$  are the voltages of the fundamental frequency and second harmonic in the output, respectively. In order to align the harmonics for pulse generation, amplitudes should satisfy  $|V_{f0}| = |V_{2f0}|$ . Therefore, according

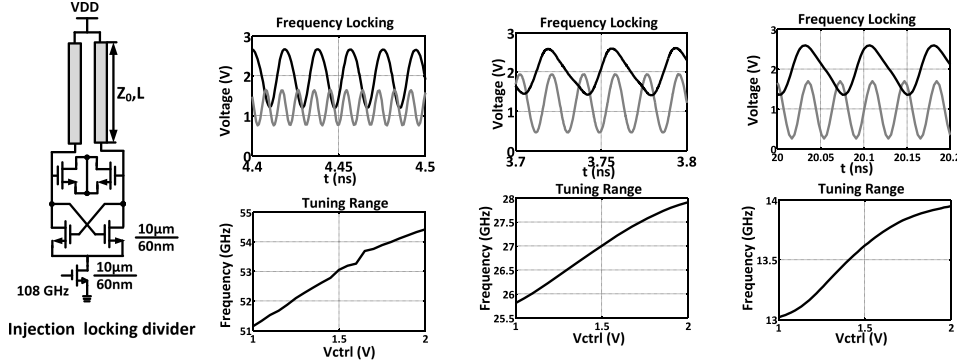


Fig. 13. Injection-locked dividers for the divider chain in the frequency synthesizer at 108 GHz and simulated results.

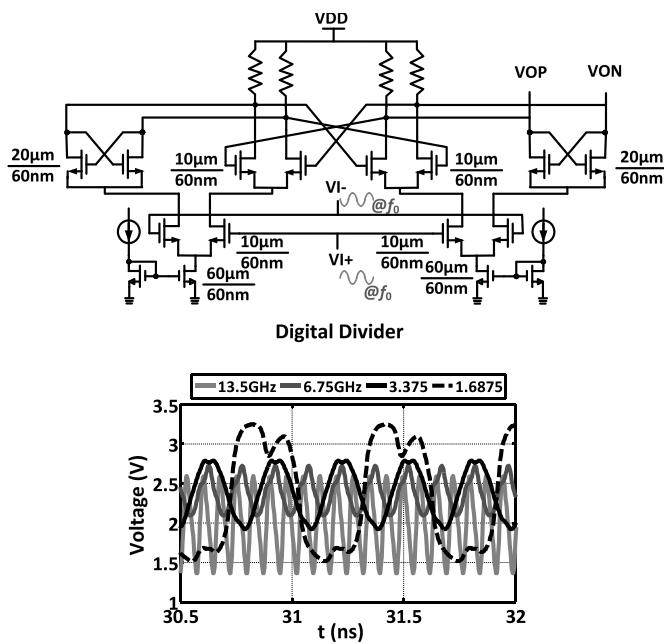


Fig. 14. Digital dividers for the divider chain in the frequency synthesizer at 108 GHz.

to (3) and (4),  $X_{f0}$  and  $X_{2f0}$  should satisfy the following equation:

$$\frac{|V_{f0}|}{|V_{2f0}|} = \frac{I_{f0}}{I_{2f0}} \sqrt{\frac{R^2}{X_{2f0}^2} + 1} = 1. \quad (5)$$

This reduces to the previous relation  $i_{f0} \sin(\psi_{f0}/2) = i_{2f0} \cos(\psi_{2f0}/2)$  when  $R = Z_0$ . The impedances presented by the current inputs and  $t$ -line are inductive and capacitive at the fundamental and second harmonic frequencies and an additional matching network is implemented between the pulse generator and the  $t$ -line to enable optimal load pull matching for an efficient second harmonic generation, as shown in Figs. 9 and 10. The simulated pulselength is approximately 2.6 ps as shown in Fig. 11. Since the architecture is optimized for pulse generation for aligning up the first two harmonics, the third harmonic generated due to suboptimal impedance at the output of the harmonic generator is not significant

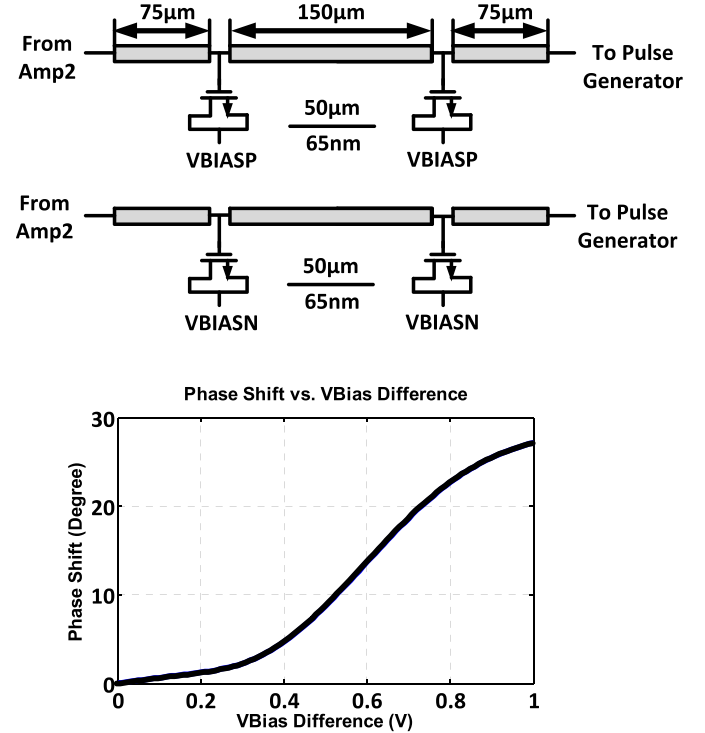


Fig. 15. Distributed delay lines and simulated delay with control voltage.

to affect the pulse shape. It is also important to understand the effect of load impedance mismatches on the combined signal shape at the output. As we will later see in the measurement results, it can be difficult to ensure optimally matched impedances at all the harmonics. Fig. 12 shows the effect on the power difference and phase offset between the two harmonics, which stays with  $\pm 1$  dB and  $\pm 10^\circ$  when measured with a single-waveguide probe capturing both signals simultaneously.

The frequency synthesizer is composed of a VCO, a divider chain, and an off-chip phase-frequency detector and a charge pump. The constituent circuit blocks are shown in Figs. 13 and 14. The VCO is implemented in a transmission-line-based cross-coupled topology with a central frequency of oscillation at 108 GHz. The divider chain is composed of three divide-by-two injection locking dividers and

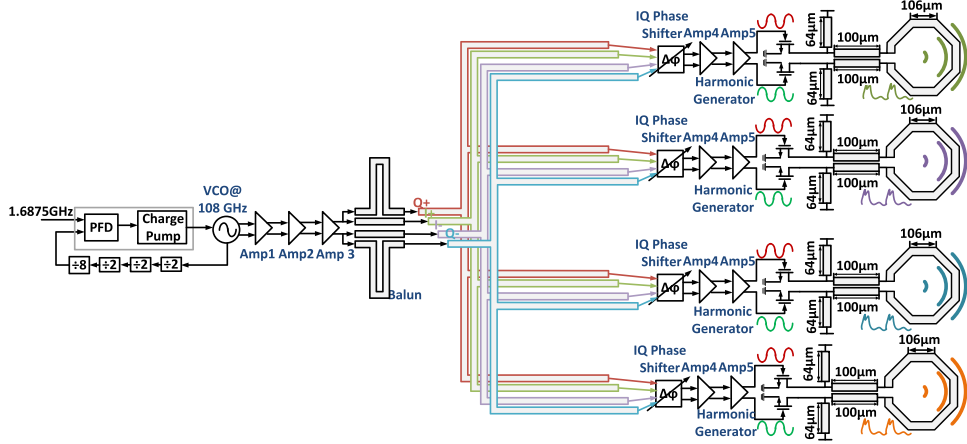


Fig. 16. Architecture of the  $4 \times 1$  array with integrated antennas for quasi-optical signal synthesis and waveform shaping by exploiting two harmonic frequencies at 108 and 216 GHz.

three digital dividers, which generate a signal of 1.6875 GHz, which is locked to the external reference. The differential amplifiers are based on the common-source topology with  $t$ -line-based matching networks and generate the drive signal with an output power of 4.6 dBm at 108 GHz to drive the nonlinear blocks. The variable delay lines are varactor-loaded  $t$ -line-based phase shifters, which can generate a maximum phase shift of around  $27^\circ$ , as shown in Fig. 15. The architecture is optimized for pulse generation through the selection of the combining  $t$ -line, and the additional phase control through the delay lines provides the opportunity to overcome process variations, mismatches, modeling inaccuracies, and dispersion, as illustrated in more detail in Section IV with measurement over multiple dies.

#### B. $4 \times 1$ Array for Quasi-Optical, Multi-harmonic, and Reconfigurable Waveform Synthesis and Shaping

The architecture for reconfigurable periodic waveform with integrated radiators is shown in Fig. 16. Similar to the on-chip picosecond pulse generator, the architecture exploits two harmonic frequencies at 108 and 216 GHz but employs four independent channels, thereby enabling complete control of amplitudes and phases of the constituent harmonics in the synthesized free-space signal. The frequency synthesizer generates differential signals at 108 GHz, which is amplified and distributed through  $\lambda/4$   $t$ -lines to generate differential quadrature signals that are distributed into four channels. In each channel, the signal is phase rotated with  $IQ$  (in phase and quadrature phase) active phase shifters and then amplified to drive two pseudo-differential harmonic generators. The nonlinear active devices in each channel drive an integrated loop antenna with a modified ground aperture, which radiates both the harmonic frequencies from chip. This allows the signals radiated from the four channels to quasi-optically combine in the far field. In this architecture, the ability to reconfigure the amplitudes and phases of the harmonics of the radiated fields enables compensation for the dispersion in the radiation path, process variations, and mismatches.

The circuit schematics of the on-chip frequency synthesizer components such as VCO, frequency dividers, and the amplifiers are similar to the ones described in Figs. 13 and 14. The  $IQ$  phase shifter, as presented in Fig. 17, is a Gilbert cell, which allows control on the amplitudes of the constituent  $IQ$  signals at the output to achieve phase rotation. The on-chip loop antenna with a modified ground aperture and the harmonic generator are co-designed to optimize the power delivered at the two harmonic frequencies at 108 and 216 GHz. Since we are interested in the control of far field of the two harmonics, it is important to ensure that the fields are not distorted significantly in the radiation path. Therefore, the radiation patterns and the broadside directivities for both harmonics should be similar. The antenna is realized on the top metal layer on a 250- $\mu\text{m}$ -thick grounded silicon substrate with bulk resistivity ( $\sigma_{\text{bulk}} \sim 13.5 \Omega \cdot \text{cm}$ ). Since the substrate is grounded, the standard silicon substrate thickness of 250  $\mu\text{m}$  implies an effective round-trip phase rotation of  $41^\circ$  at 107 GHz and  $-95^\circ$  at 214 GHz.<sup>2</sup> Therefore, the magnitudes of the radiated fields for both frequencies are not significantly affected and the antenna demonstrates broadside radiation patterns at both frequencies. Fig. 18 shows the simulated patterns and maximum directivities of 8.0 and 7.2 dB for 108 and 216 GHz, respectively. The matching network is designed to enable simultaneous impedance transformations at both the harmonics as shown in Fig. 19.

#### IV. MEASUREMENT SETUPS AND RESULTS

The chips are fabricated in a 65-nm LP-CMOS process with  $f_{\text{max}} \sim 190$  GHz. To demonstrate the waveform reconfigurability of the output signal, ideally time-domain measurements should be carried out. However, in the absence of a sampling scope with a bandwidth more than 220 GHz, measurements are performed in frequency domain with

<sup>2</sup>The mode wavelengths in the substrata are not  $\lambda_0/\sqrt{\epsilon_{\text{Si}}}$ . However, it can be shown that the radiation efficiency is maximized when the following condition is satisfied:  $2h/\lambda_{\text{f0}} + 180^\circ \sim 360^\circ$  [37].

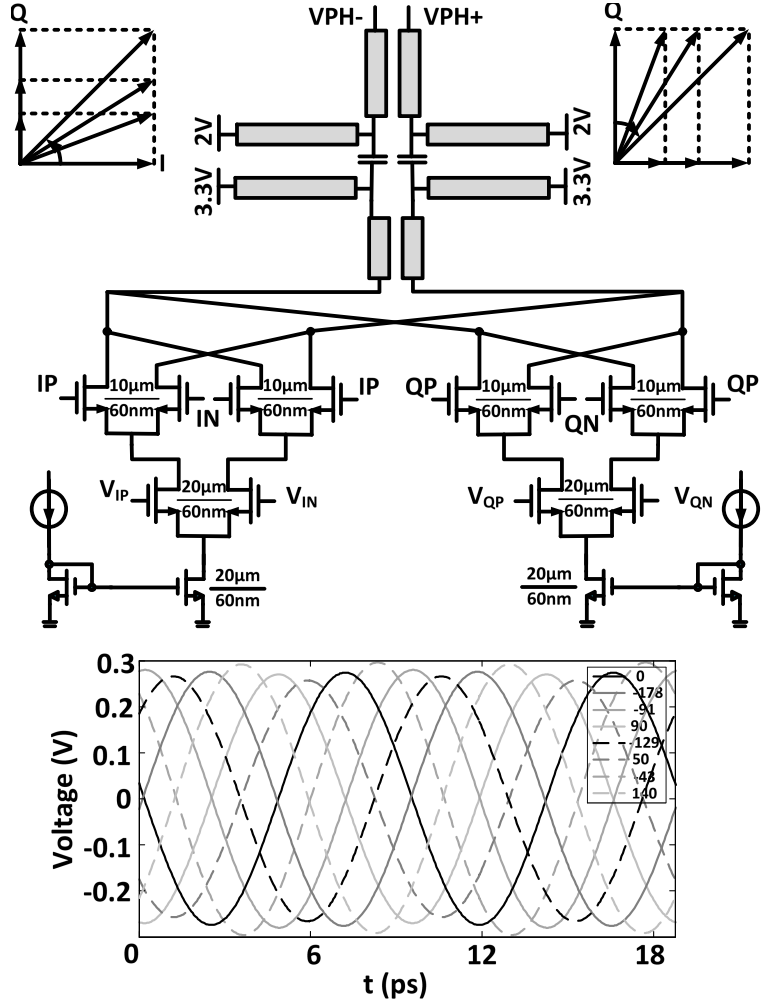


Fig. 17. Circuit schematic of *IQ* phase shifter.

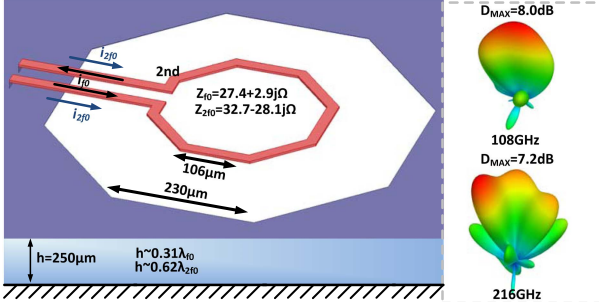


Fig. 18. Integrated on-chip loop antenna design and simulation of radiation patterns at both harmonics.

custom measurement setups capable of capturing both amplitude and phase offsets of both the harmonics simultaneously.

#### A. Measurement of On-Chip Picosecond Pulse Generator

The die micrograph of the on-chip picosecond pulse generator is shown in Fig. 20. The chip occupies an area of  $1.1 \text{ mm} \times 2.3 \text{ mm}$ .

In order to measure the time-domain signal at the output of the integrated architecture, both the harmonic frequencies

need to be tapped and measured simultaneously for power and phase offset. This is important because while individual power measurements for each harmonic can be done in succession, the phase offset measurement needs simultaneous capturing of both the frequencies. Fig. 21 shows the custom measurement setup where signals from both the pads are captured by 110–170-GHz waveguide-based probes to capture the first and second harmonic signals simultaneously.<sup>3</sup> As shown in Fig. 21, one of the probes is connected to the Erickson PM4 power meter through a WR 6–WR 10 taper to measure the total power of the signal. The other output of the probe is connected to a receiver path, which consists of *D*-band harmonic mixer, diplexer, splitter and amplifiers to downconvert both the fundamental and second harmonic frequencies simultaneously to a range between DC and 2 GHz, which is the bandwidth of the diplexer. This is achieved by choosing the local oscillator (LO)

<sup>3</sup>In the absence of a probe that operates in single mode for both the harmonics, overmoded operation was unavoidable. However, the effect was taken into account during the calibration process. The TE<sub>10</sub> cut-off mode for the *D*-band probe is 90.85 GHz, which therefore allows propagation of the 105-GHz component. At 214 GHz, higher order modes can be excited [ $f_c(\text{TE}_{20}) = f_c(\text{TM}_{10}) = 203 \text{ GHz}$ ] and the spectral region corresponding to this overmoded region was measured multiple times to ensure stability of the measurement.

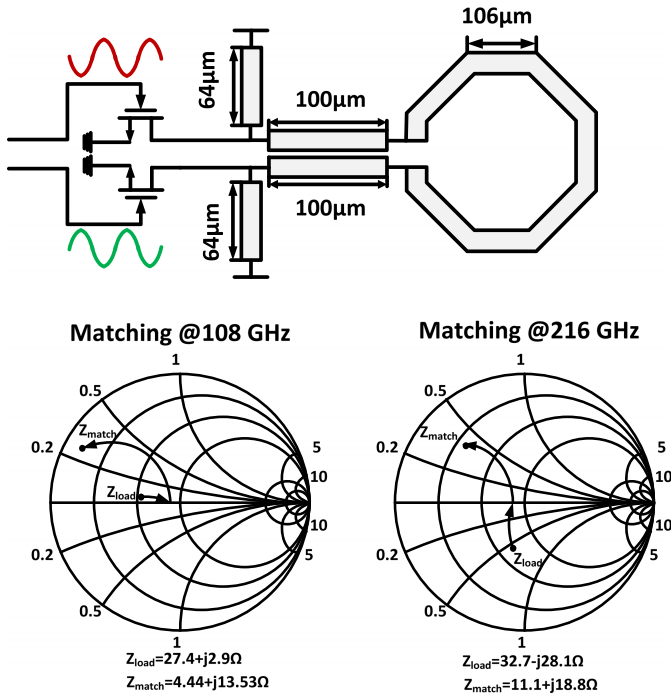


Fig. 19. Simultaneous matching from the loop antenna to the nonlinear block for both harmonics.

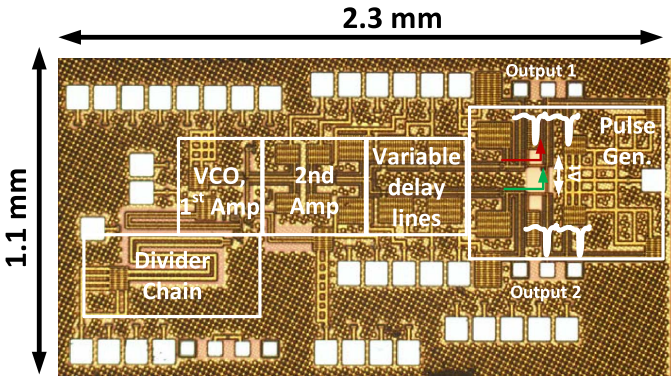


Fig. 20. Chip micrograph and circuit block placement of the on-chip picosecond pulse generator.

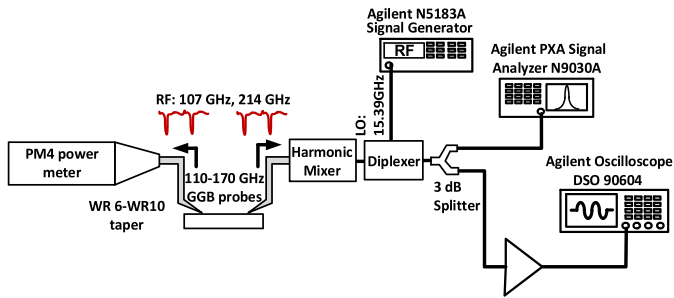


Fig. 21. Frequency-domain measurement setup to capture time-domain waveforms at 107 and 214 GHz by measuring the amplitudes and phase offset of the fundamental and the second harmonic signals simultaneously.

signal judiciously at 15.39 GHz and exploiting the 7th and 14th harmonics of the mixer to downconvert the two RFs to 0.8 and 1.6 GHz, respectively. This allows the IF that contains information for both the signals to be measured simultaneously

for power and phase offset ( $2\theta_{f0} - \theta_{2f0}$ ). The IF signal is split into two paths to measure the frequency components in a spectrum analyzer and a real-time scope after amplified by an LNA to measure the phase offset. The measured RFs are at 107 and 214 GHz.

Amplitude calibration for the spectral components is carried as follows. First, the scattering parameters of the probe are measured from 70 to 220 GHz in a vector network analyzer, which captures the amplitude and phase response of the probes across the frequency of interest. Next, the losses induced by the harmonic mixer, diplexer, and the splitter and the cable assembly are calibrated by injecting known power into the input of the mixer at both the fundamental and second harmonic frequencies and observing the IF power. A more challenging calibration is to characterize the phase accumulated by the IF frequencies generated by mixing the 107 and 214 GHz with the LO harmonics, as it propagates from the mixer through the receiver chain to the oscilloscope. The details are shown in Fig. 22. This calibration of the phase offset is carried by exploiting the nonlinearity of the harmonic mixer itself. Since the mixer is a Schottky diode and has nonlinear response, it can be modeled by a nonlinear conductance and a nonlinear capacitance as shown in Fig. 22 [42]–[44], along with the other diode interconnect parasitics and matching network. During phase calibration, the mixer is excited with a pure tone at  $I_{f0} = 107$  GHz and the mixer generates the second harmonic component  $I_{2f0} = 214$  GHz in phase at the output of the modeled current source (Fig. 22) due to the dominant nonlinear conductance of the diode due to its forward bias. Both the signals at  $f_0$  and  $2f_0$  get downconverted by the input LO to  $IF_{f0}$  and  $IF_{2f0}$  and are captured by the oscilloscope. However, from the mixer to the oscilloscope, they suffer different delays due to: 1) phase difference between the LO harmonics and 2) frequency response of the passive elements in the receiver chain such as the diode capacitance, interconnect parasitics, and matching networks in the diode, diplexer, LNA, and the cable assembly. This is also the same phase suffered by the second harmonic component of a pulse train as it gets down-converted through the chain (Fig. 22). Therefore, this is the calibrated phase offset of the receiver chain and needs to be taken into account along with the probe S-parameters to measure the true phase offset of the two harmonic frequencies.

Fig. 23 shows the measured and calibrated spectra of the fundamental frequency at 107 GHz and the second harmonic at 214 GHz, demonstrating an equal output power of  $-6.4$  dBm. Fig. 24 shows the retrieved time domain waveform from the measured amplitudes and phases of the harmonics for multiple settings of the variable delay lines. The optimized pulse setting shows that the output power of both harmonics are  $-6.4$  dBm with the desirable phase relationship  $2\theta_{f0} - \theta_{2f0} = \pi$ , resulting in a pulse train with a  $-3.4$ -dBm output power and a 2.6-ps pulselwidth. As noted before, the variable delay lines allow some degree of reconfigurability of the phases and amplitudes of the spectral components. While full control for both the harmonics requires four harmonic paths, the optimized pulse generator architecture achieves partial control of the harmonic frequencies. The measured and simulated

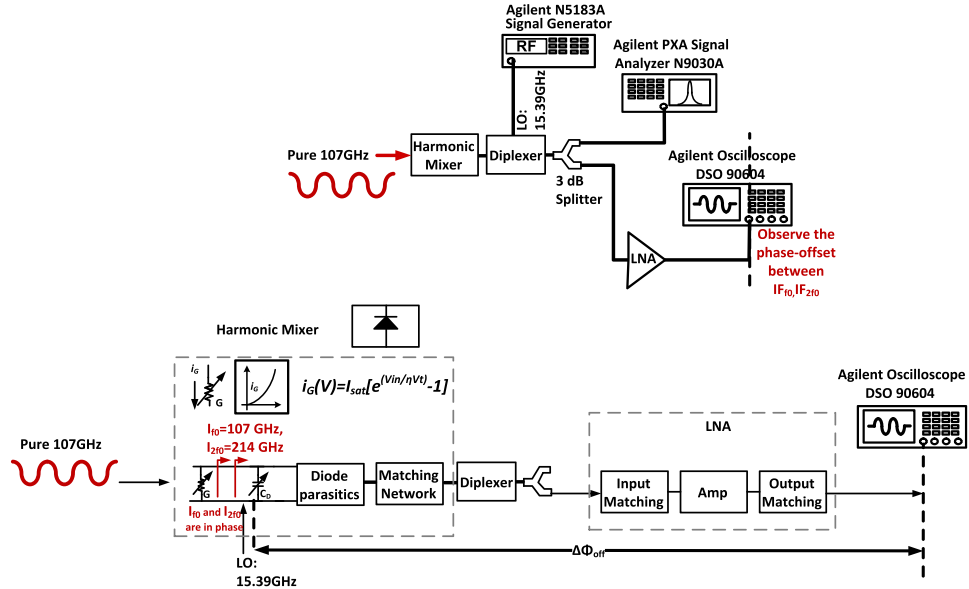


Fig. 22. Phase offset calibration at 107 and 214 GHz frequency components through the receiver path.

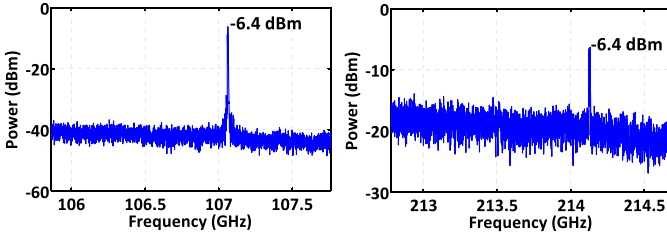


Fig. 23. Measured and calibrated power spectra of the fundamental frequency at 107 GHz and second harmonic at 214 GHz showing an almost equal power of  $-6.4 \text{ dBm}$ .

variations of the output powers of both harmonics and phase offset between the two harmonics are shown in Fig. 25. The phase offset ( $2\theta_{f0} - \theta_{2f0}$ ) can be approximately varied from  $175^\circ$  to  $230^\circ$ . The fundamental frequency can either have larger or smaller power than the second harmonic. These variations enable dynamic reconfiguration of the output time domain waveforms.

Fig. 26 shows the VCO tuning range and phase noise of both harmonics of the pulse train with the free-running VCO. The VCO can be tuned from 106.5 to 108.3 GHz. The phase noise of the fundamental frequency shows  $-70 \text{ dBc/Hz}$  at a 1-MHz offset, which is 6 dB lower than the second harmonic component as expected. Fig. 27 demonstrates the powers of both harmonic frequencies and phase offsets for four different chips under nominal control voltage settings. The maximum power difference between the fundamental frequency and the second harmonic signal of the four chips is less than 1 dB. The phase offsets of the four chips are within the range of  $178^\circ$ – $187^\circ$ . It demonstrates the robustness of the architecture to process variations. To the best of the authors' knowledge, this paper generates the sharpest pulse on-chip in integrated circuit technology with the capability of the dynamic reconfiguration.

### B. Measurement of $4 \times 1$ Array for Quasi-Optical Waveform Synthesis and Shaping

The die micrograph of the  $4 \times 1$  array for quasi-optical dynamic waveform synthesis and shaping is shown in Fig. 28. The chip has a size of  $2.7 \text{ mm} \times 3.1 \text{ mm}$ . The chip is mounted vertically with an FR-4 PCB and the radiated signals are captured from the front side. No substrate thinning of silicon lens is employed for the radiated field measurement. The downconversion receiver architecture to measure the amplitude and phase offset of the radiated harmonics is shown in Fig. 29. Both the RFs are captured simultaneously by a 110–170-GHz horn antenna and downconverted by the 7th and 14th harmonic of the LO at 15.5 GHz to observe for the IF frequencies simultaneously. The measured RFs are at 107.5 and 215 GHz. The IF signal that contains information of both harmonics passes through a splitter to a spectrum analyzer and a real-time scope after amplified by three LNAs. Similar to the previous method, the entire path is calibrated for both amplitude and phase offset following the same methodology for the programmable picosecond pulse generator.

The measured calibrated spectra of both harmonic frequencies at 107.5 and 215 GHz are shown in Fig. 30, indicating an EIRP of  $4.6 \text{ dBm}$  for 107.5 GHz and an EIRP of  $5.0 \text{ dBm}$  for 215 GHz, respectively, when all the antennas are driven in phase. Fig. 31 demonstrates the radiation patterns in azimuth and elevation at both 107.5 and 215 GHz. The maximum directivities are approximately 7.6 and 9 dB for 107.5 and 215 GHz, respectively. The measured tuning range and phase noise of the radiated 107.5 and 215 GHz signals with the free-running VCO are shown in Fig. 32. The VCO can be tuned from 107.0 to 108.1 GHz. The phase noise of the fundamental frequency at 107 GHz is  $-75 \text{ dBc/Hz}$  at a 1-MHz offset expectedly 6 dB lower than the corresponding second harmonic signal at 214 GHz.

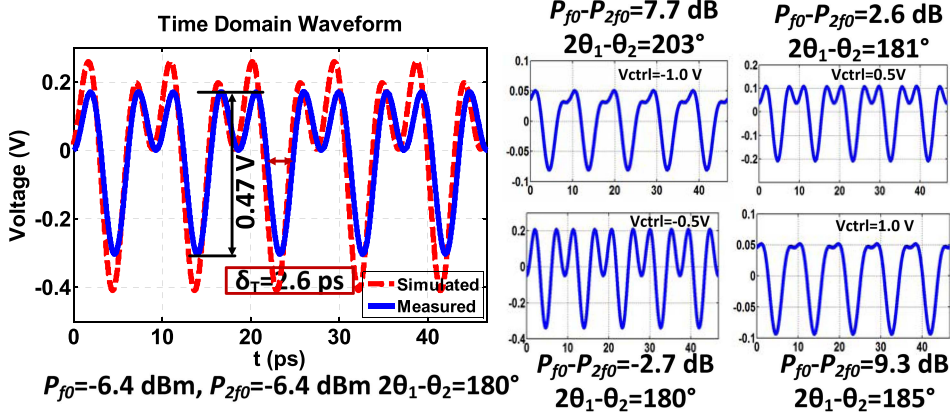


Fig. 24. Measured time-domain waveforms for five different settings of the controllable delay lines. The optimized pulse train shows 2.6-ps pulsewidth.

TABLE I  
CHIP PERFORMANCE WITH THE PRIOR-ART-ON-SILICON-BASED ARCHITECTURES FOR PULSE GENERATION

Parameter	This work	[29]	[30]	[33]	[34]	[35]	[36]
Shortest Pulse width (ps)	2.6	9.6	18	26	8	45 ++	5.5
Waveform Reconfigurability	Yes	No	No	No	No	No	No
On-chip/radiated	On-chip/ Rad.	On-chip	On-chip.	Rad.	Rad.	Rad.	On-chip.
Measurement method	Freq. domain	Time domain	Time domain	Time and Freq. domain	Time domain	Freq. Domain	
Beam-steering	Yes (4x1 array)	N/A	N/A	No	No	No	N/A
Pulse Gen. Method	Multi-harmonic signal combination	Nonlinear lattice	Mode-locked oscillator	Oscillator switching	Digital pulse	Oscillator switching	Nonlinear t-line
Power/EIRP	-3.4 dBm (onchip)/ -3.2 dBm (EIRP with no lens)	~6 dBm*	-4.5 dBm (@f <sub>0</sub> =18.7 GHz)	13 (EIRP with no lens)	13 (EIRP with Si Lens)	15.7 (EIRP with Si Lens)	15.8 dBm**
Technology	65 nm LP CMOS	0.13μm CMOS	GaAs	0.13μm SiGe	0.13μm SiGe	65 nm bulk CMOS	GaAs

\* Estimated from measured 1.3Vp-p over a 50 Ω load. Input signal is provided at 20 GHz from a 34 dBm PA.

\*\* Estimated from measured 3.9Vp-p over a 50 Ω load. Input signal is provided at 20 GHz with 20 dBm input power

++ Simulated

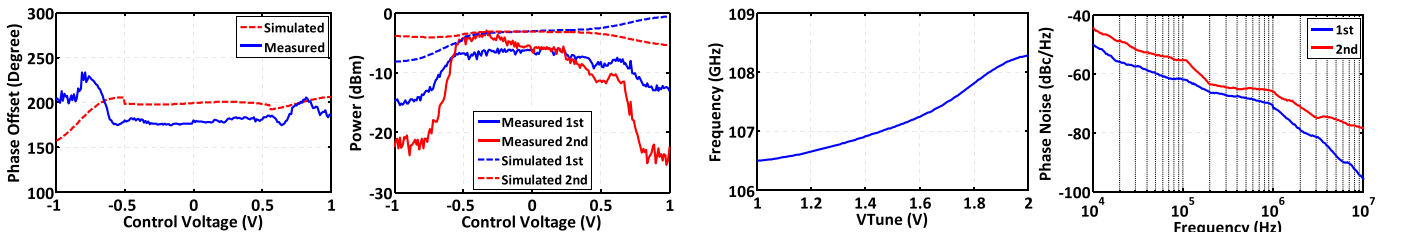


Fig. 25. Measured and simulated variations of phase relationship and amplitudes of the fundamental frequency at 107 GHz and the second harmonic at 214 GHz with the change of the variable delay line settings.

Quasi-optical signal generation, synthesis, and reconfiguration are achieved through phase controls at the fundamental frequency in the four channels. The architecture allows radiation of any arbitrary combination of the harmonic frequencies with the desirable amplitude and phase relationship. Due to the inability to visualize the possible reconfiguration with all the four control voltages, we show a subset of the measured variations of the amplitudes and relative phase offsets between

Fig. 26. Measured frequency tuning and phase noise of both harmonics components of the pulse train with a free-running VCO for the on-chip picosecond pulse generator.

the radiated far-field signals at 107.5 and 215 GHz in Fig. 33. This is measured by varying the phase rotator settings in the first and second channels for three different phase settings of the fourth channel. The first and second rows show the measured variation of the magnitude of the far field at  $f_0$  and  $2f_0$ , respectively, while the third row depicts that of the phase offset ( $2\theta_{f0} - \theta_{2f0}$ ). As shown in Fig. 33, the expected rotations and amplitude variation of the radiated

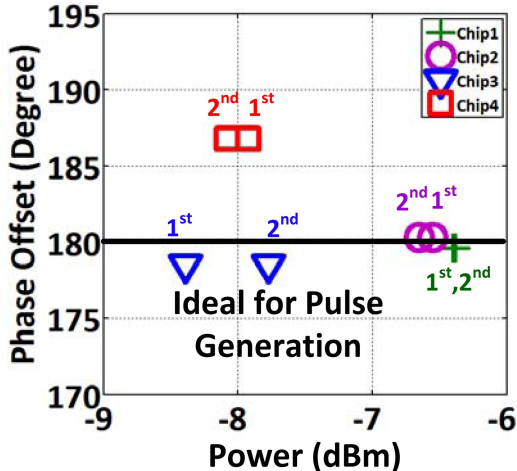


Fig. 27. Measured harmonic powers and phase offsets for four different chips under normal delay control settings.

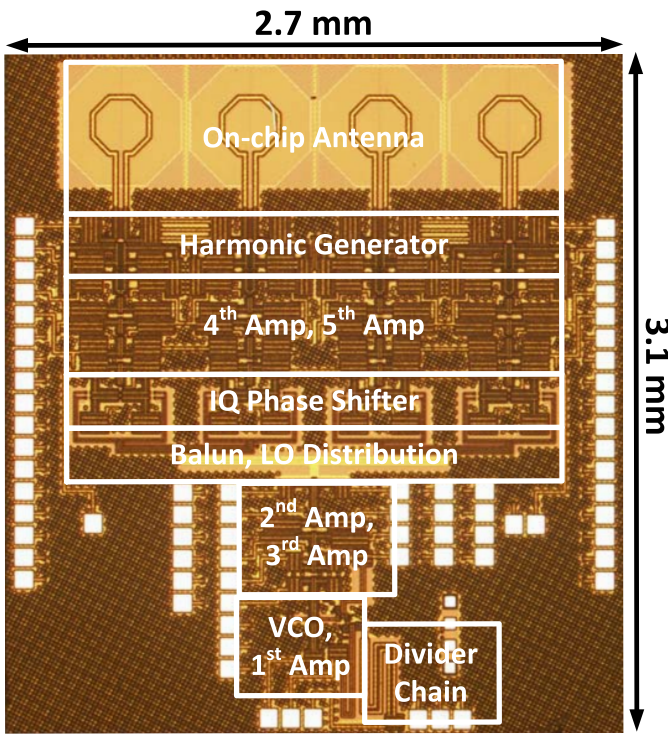


Fig. 28. Chip micrograph and circuit block placement of the  $4 \times 1$  array for quasi-optical signal synthesis and dynamic waveform shaping.

fields ( $E_{f_0}$ ,  $E_{2f_0}$ ) for different regions match closely with the measured power spectra. Six representative examples of the measured periodic waveforms are shown in Fig. 33. As an example, a pulse train is radiated with a pulsedwidth of 2.6 ps and a  $-3.2$ -dBm EIRP. This is achieved (from Fig. 33) when the electric fields of the two radiated harmonics align in amplitude and phase. In addition, other combinations of the two harmonic frequencies are possible to generate with the various phase rotator settings such as pure tone radiations with 1.4- and 2.1-dBm EIRPs at 107.5 and 215 GHz. The custom frequency-domain measurement setup that captures complex spectral information enables us to overcome the

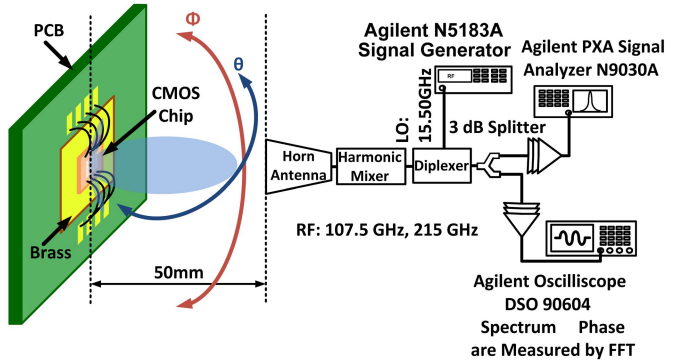


Fig. 29. Measurement setup to capture the radiated time-domain fields and radiation patterns at 107.5 and 215 GHz by measuring the amplitudes and phases of the fundamental and second harmonic signals.

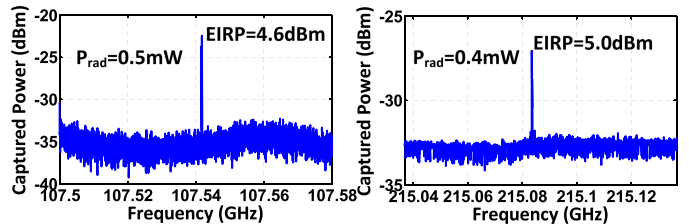


Fig. 30. Measured power spectra of the radiated signal with simultaneous harmonic contents at 107.5 and 215 GHz.

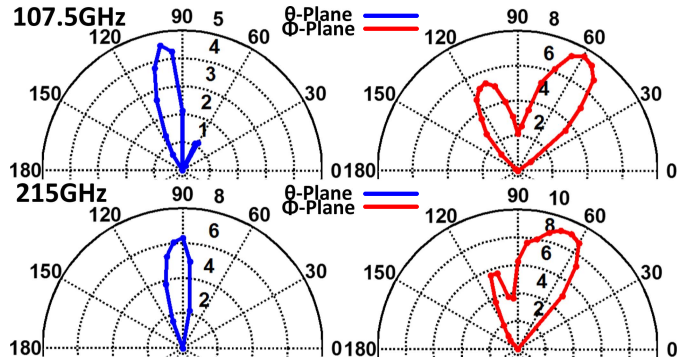


Fig. 31. Measured radiation patterns of the signal with simultaneous harmonic contents at 107.5 and 215 GHz.

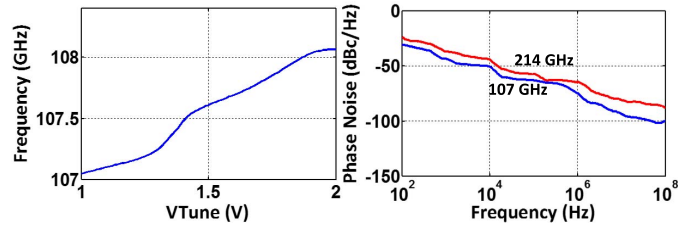


Fig. 32. Measured frequency tuning of the central VCO and the measured phase noise of the radiated harmonic components with the free-running VCO for the array chip.

bandwidth limitations of real-time scopes or sampling scopes and measure time-domain signals occupying spectrum more than one waveguide band. While the pulse train is constructed quasi-optically in an intended direction, the time-domain waveform will change as the measured direction moves away in azimuth and elevation. Fig. 34 shows the slight pulse degradation measured away from the broadside axis by  $+5^\circ$

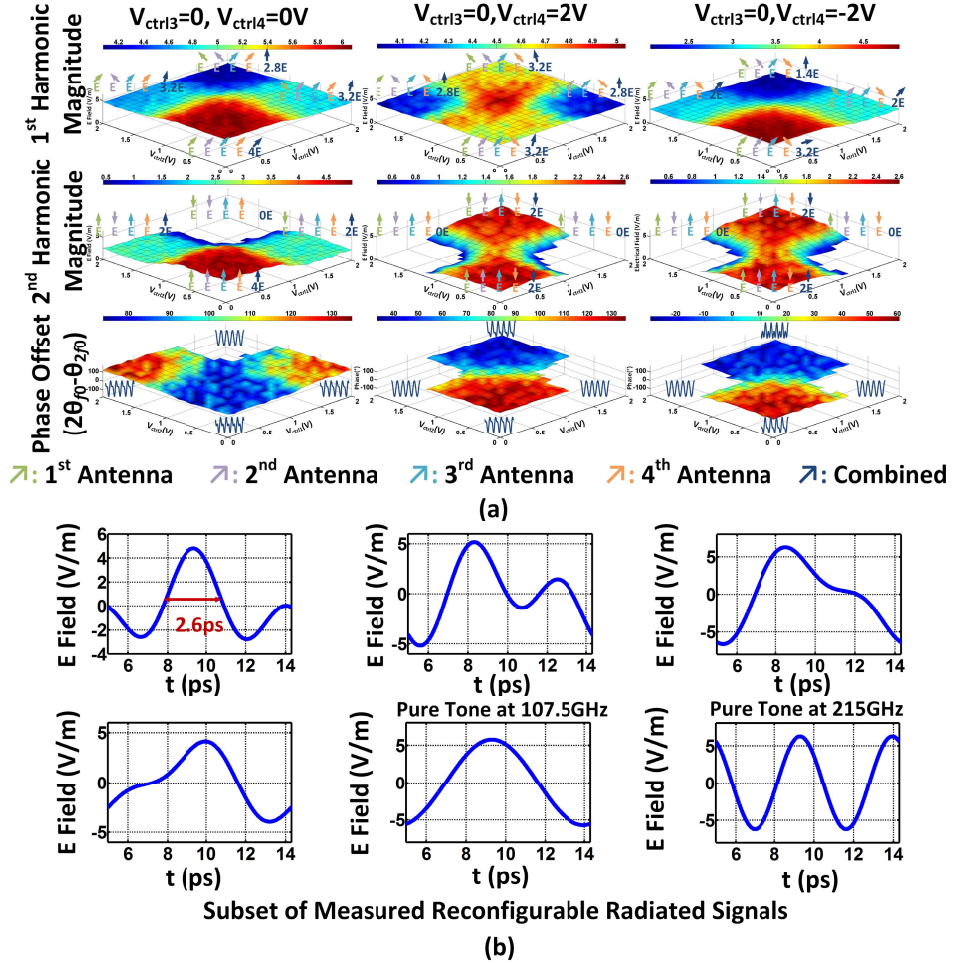


Fig. 33. (a) Measured variation of the amplitudes and phases of the radiated far field at the fundamental frequency  $f_0$  at 107.5 GHz and second harmonic  $2f_0$  at 215 GHz. This is measured by variation of the phase rotator settings in the first and second channels for three different phase settings of the fourth channel. The expected rotations of the radiated fields ( $E_{f0}, E_{2f0}$ ) of both the harmonics along with their time signatures are drawn in the figure. (b) Measured subset of the possible reconfigurable time-domain waveforms.

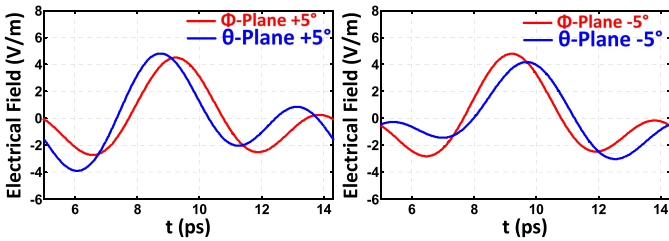


Fig. 34. Time-domain waveforms away from the broadside axis demonstrating slight pulse degradation.

and  $-5^\circ$ . As illustrated in (2), the phase control settings can be reconfigured in order to direct the desired signal waveform in a different direction, while in other directions, the signal spectra will vary. This is not an issue for applications such as spectroscopy where the material under test is located at a fixed position and radiated with picosecond pulses to observe internal molecular resonances.

The chip consumes 388 mW of DC power in the frequency synthesizer and amplifiers in the central path and 178 mW in each channel. Table I compares the chip performance with prior work on silicon-based architectures for pulse generation. To the best of the authors' knowledge, this is the sharpest

radiated pulse demonstrated in any IC technology with the capability of dynamic waveform shaping. The architecture when combined with programmable repetition frequency (Fig. 1) can open the door to innovations in broadband terahertz imaging, sensing, and spectroscopy.

## V. CONCLUSION

This paper presents a scalable architecture in silicon that allows synthesis and dynamic waveform shaping of periodic mm-Wave signals, either generated on-chip or quasi-optically through radiation in free space capable of producing pulse trains with picosecond time signatures. This is achieved by allowing electromagnetic fields of fundamental and multiple harmonic frequencies to combine with precise amplitudes and delays to enable reconfigurable waveform synthesis. The first example presented is where the signal synthesis is achieved on-chip on a transmission line that achieves amplitude and phase alignment of two harmonic frequencies at 107 and 214 GHz, demonstrating a pulse train at the output with a measured pulselength of 2.6 ps and a 0.46-mW output power. Next, a four-element array with integrated antennas is presented, which is demonstrated to

radiate pulse trains of 2.6-ps time widths as well as pure tones and harmonic frequencies at 107.5 GHz (EIRP = 4.6 dBm), 215 GHz (EIRP = 5.0 dBm), and any combination of amplitudes and delays of these two harmonics to generate a set of reconfigurable waveforms in free space. No silicon lens or substrate thinning was employed. To the best of the authors' knowledge, this is the sharpest radiated pulses demonstrated in any IC technology and the first demonstration of dynamic waveform shaping of radiated picosecond time signatures, which can open the door to innovations in broadband terahertz imaging, sensing, and spectroscopy.

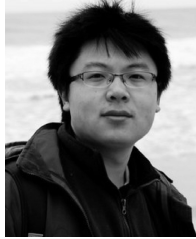
### ACKNOWLEDGMENT

The authors would like to thank the National Science Foundation and Dr. W. Chappell, Defense Advanced Research Projects Agency, for providing fabrication opportunity and all members of the Integrated Microsystems Research Laboratory, Princeton, for technical discussion.

### REFERENCES

- [1] M. Tonouchi, "Cutting-edge Terahertz Technology," *Nature Photon.*, vol. 1, pp. 97–105, Feb. 2007.
- [2] I. Duling and D. Zimdars, "Terahertz imaging: Revealing hidden defects," *Nature Photon.*, vol. 3, pp. 630–632, Nov. 2009.
- [3] P. H. Siegel, "Terahertz technology," *IEEE Trans. Microw. Theory Techn.*, vol. 50, no. 3, pp. 910–928, Mar. 2002.
- [4] P. H. Siegel, "Terahertz technology in biology and medicine," *IEEE Trans. Microw. Theory Techn.*, vol. 52, no. 10, pp. 2438–2447, Oct. 2004.
- [5] R. Hadi *et al.*, "A 1 k-pixel video camera for 0.7–1.1 terahertz imaging applications in 65-nm CMOS," *IEEE J. Solid-State Circuits*, vol. 47, no. 12, pp. 2999–3012, Dec. 2012.
- [6] K. Sengupta, D. Seo, L. Yang, and A. Hajimiri, "Silicon integrated 280 GHz imaging chipset with 4×4 SiGe receiver array and CMOS source," *IEEE Trans. THz Sci. Technol.*, vol. 5, no. 3, pp. 427–437, May 2015.
- [7] K. Sengupta, D. Seo, and A. Hajimiri, "A terahertz imaging receiver in 0.13 μm SiGe BiCMOS technology," in *Proc. 36th Int. Conf. Infr. Millim. Terahertz Waves (IRMMW-THz)*, Oct. 2011, pp. 1–2.
- [8] E. Seok *et al.*, "A 410GHz CMOS push-push oscillator with an on-chip patch antenna," in *IEEE Int. Solid-State Circuits Conf. Dig. Tech. Papers*, San Francisco, CA, USA, Feb. 2008, pp. 472–629.
- [9] D. Shim, D. Koukis, D. J. Arenas, D. B. Tanner, and K. O. Kenneth, "553-GHz signal generation in CMOS using a quadruple-push oscillator," in *VLSI Circuits Symp. Dig.*, Jun. 2011, pp. 154–155.
- [10] K. Sengupta and A. Hajimiri, "Distributed active radiation for THz signal generation," in *IEEE ISSCC Dig. Tech. Papers*, Feb. 2011, pp. 288–289.
- [11] K. Sengupta and A. Hajimiri, "A 0.28 THz 4×4 power-generation and beam-steering array," in *IEEE Int. Solid-State Circuits Conf. (ISSCC) Dig. Tech. Papers*, Feb. 2012, pp. 256–258.
- [12] D. Huang *et al.*, "324GHz CMOS frequency generator using linear superposition technique," in *IEEE Int. Solid-State Circuits Conf. Dig. Tech. Papers*, San Francisco, CA, USA, Feb. 2008, pp. 476–629.
- [13] K. Sengupta and A. Hajimiri, "A 0.28 THz power-generation and beam-steering array in Cmos based on distributed active radiators," *IEEE J. Solid-State Circuits*, vol. 47, no. 12, pp. 3013–3031, Dec. 2012.
- [14] K. Sengupta and A. Hajimiri, "Mutual synchronization for power generation and beam-steering in CMOS with on-chip sense antennas near 200 GHz," *IEEE Trans. Microw. Theory Techn.*, vol. 63, no. 9, pp. 2867–2876, Sep. 2015.
- [15] K. Sengupta and A. Hajimiri, "Sub-THz beam-forming using near-field coupling of distributed active radiator arrays," in *Proc. IEEE Radio Freq. Integr. Circuits Symp.*, Jun. 2011, pp. 1–4.
- [16] K. Sengupta and A. Hajimiri, "Designing optimal surface currents for efficient on-chip mm-wave radiators with active circuitry," *IEEE Trans. Microw. Theory Techn.*, vol. 64, no. 7, pp. 1976–1988, Jul. 2016.
- [17] O. Momeni and E. Afshari, "High power terahertz and millimeter-wave oscillator design: A systematic approach," *IEEE J. Solid-State Circuits*, vol. 46, no. 3, pp. 583–597, Mar. 2011.
- [18] J. Sharma and H. Krishnaswamy, "216-and 316-GHz 45-nm SOI CMOS signal sources based on a maximum-gain ring oscillator topology," *IEEE Trans. Microw. Theory Techn.*, vol. 61, no. 1, pp. 492–504, Jan. 2013.
- [19] Y. Tousi and E. Afshari, "A scalable THz 2D phased array with +17dBm of EIRP at 338GHz in 65nm bulk CMOS," in *IEEE Int. Solid-State Circuits Conf. (ISSCC) Dig. Tech. Paper*, Feb. 2014, pp. 258–259.
- [20] R. Han and E. Afshari, "A 260GHz broadband source with 1.1mW continuous-wave radiated power and EIRP of 15.7dBm in 65nm CMOS," in *IEEE Int. Solid-State Circuits Conf. (ISSCC) Dig. Tech. Paper*, Feb. 2013, pp. 138–139.
- [21] J. Grzyb, Y. Zhao, and U. Pfeiffer, "A 288-GHz lens-integrated balanced triple-push source in a 65-nm CMOS technology," *IEEE J. Solid-State Circuits*, vol. 48, no. 7, pp. 1751–1761, Jul. 2013.
- [22] K. Schmalz, R. Wang, J. Borngraber, W. Debski, W. Winkler, and C. Meliani, "245 GHz SiGe transmitter with integrated antenna and external PLL," in *Proc. IEEE Int. Microw. Symp.*, Seattle, WA, USA, Jun. 2013, pp. 1–3.
- [23] U. Pfeiffer *et al.*, "A 0.53THz reconfigurable source array with up to 1mW radiated power for terahertz imaging applications in 0.13 μm SiGe BiCMOS," in *IEEE Int. Solid-State Circuits Conf. Dig. Tech. Papers*, San Francisco, CA, USA, Feb. 2014, pp. 256–257.
- [24] R. Han *et al.*, "A 320GHz phase-locked transmitter with 3.3mW radiated power and 22.5dBm EIRP for heterodyne THz imaging systems," in *IEEE Int. Solid-State Circuits Conf. Dig. Tech. Papers*, San Francisco, CA, USA, Feb. 2015, pp. 1–3.
- [25] P. Y. Chiang, Z. Wang, O. Momeni, and P. Heydari, "A 300GHz frequency synthesizer with 7.9% locking range in 90nm SiGe BiCMOS," in *IEEE Int. Solid-State Circuits Conf. Dig. Tech. Papers*, San Francisco, CA, USA, Feb. 2014, pp. 260–261.
- [26] J.-D. Park, S. Kang, and A. M. Niknejad, "A 0.38THz fully integrated transceiver utilizing quadrature push-push circuitry," in *Symp. VLSI Circuits Dig.*, Jun. 2011, pp. 22–23.
- [27] Q. J. Gu *et al.*, "CMOS THz generator with frequency selective negative resistance tank," *IEEE Trans. THz Sci. Technol.*, vol. 2, no. 2, pp. 193–202, Mar. 2012.
- [28] H. A. Haus, "Mode-locking of lasers," *IEEE J. Sel. Topics Quantum Electron.*, vol. 6, no. 6, pp. 1173–1185, Nov./Dec. 2000.
- [29] W. Lee, M. Adnan, O. Momeni, and E. Afshari, "A nonlinear lattice for high-amplitude picosecond pulse generation in CMOS," *IEEE Trans. Microw. Theory Techn.*, vol. 60, no. 2, pp. 370–380, Feb. 2012.
- [30] O. O. Yildirim, D. Ha, and D. Ham, "Fully monolithic 18.7GHz 16ps GaAs mode-locked oscillators," in *Proc. IEEE RFIC Symp.*, Jun. 2011, pp. 1–4.
- [31] E. Afshari and A. Hajimiri, "Nonlinear transmission lines for pulse shaping in silicon," *IEEE J. Solid-State Circuits*, vol. 40, no. 3, pp. 744–752, Mar. 2005.
- [32] M. Case, M. Kamegawa, R. Yu, M. J. W. Rodwell, and J. Franklin, "Impulse compression using soliton effects in a monolithic GaAs circuit," *Appl. Phys. Lett.*, vol. 58, no. 2, pp. 173–175, Jan. 1991.
- [33] A. Arbabian, S. Callender, S. Kang, M. Rangwala, and A. M. Niknejad, "A 94 GHz mm-wave-to-baseband pulsed-radar transceiver with applications in imaging and gesture recognition," *IEEE J. Solid-State Circuits*, vol. 48, no. 4, pp. 1055–1071, Apr. 2013.
- [34] M. M. Assefzadeh and A. Babakhanji, "An 8-psec 13dBm peak EIRP digital-to-impulse radiator with an on-chip slot bow-tie antenna in silicon," in *IEEE MTT-S Int. Microw. Symp. Dig.*, Jun. 2014, pp. 1–4.
- [35] R. Han and E. Afshari, "A CMOS high-power broadband 260-GHz radiator array for spectroscopy," *IEEE J. Solid-State Circuits*, vol. 48, no. 12, pp. 3090–3104, Dec. 2013.
- [36] M. Case, M. Kamegawa, R. Yu, M. J. W. Rodwell, and J. Franklin, "Impulse compression using soliton effects in a monolithic GaAs circuit," *Appl. Phys. Lett.*, vol. 58, no. 2, pp. 173–175, Jan. 1991.
- [37] W. B. Dou and Z. L. Sun, "Surface wave fields and power in millimeter wave integrated dipole antennas," *Int. J. Inf. Millim. Waves*, vol. 18, no. 3, pp. 711–721, Mar. 1997.
- [38] X. Wu and K. Sengupta, "Programmable picosecond pulse generator in CMOS," in *Proc. IEEE MTT-S Int. Microw. Symp.*, May 2015, pp. 1–4.
- [39] X. Wu and K. Sengupta, "Dynamic waveform shaping for reconfigurable radiated periodic signal generation with picosecond time-widths," in *Proc. IEEE CICC*, Sep. 2015, pp. 1–4.
- [40] X. Wu and K. Sengupta, "A 40-to-330GHz synthesizer-free THz spectroscope-on-chip exploiting electromagnetic scattering," in *IEEE Int. Solid-State Circuits Conf. Dig. Tech. Papers*, Feb. 2016, pp. 428–429.

- [41] X. Wu and K. Sengupta, "On-chip THz spectroscope exploiting electromagnetic scattering with multi-port antenna," *IEEE J. Solid-State Circuits*, vol. PP, no. 99, Dec. 2016, doi: 10.1109/JSSC.2016.2597845.
- [42] A. V. Raisanen, "Frequency multipliers for millimeter and submillimeter wavelengths," *Proc. IEEE*, vol. 80, no. 11, pp. 1842–1852, Nov. 1992.
- [43] J. T. Louhi and A. V. Raisanen, "On the modeling and optimization of Schottky varactor frequency multipliers at submillimeter wavelengths," *IEEE Trans. Microw. Theory Techn.*, vol. 43, no. 4, pp. 922–926, Apr. 1995.
- [44] G. Emili, F. Alimenti, P. Mezranotte, L. Roselli, and R. Sorrentino, "Rigorous modeling of packaged Schottky diodes by the nonlinear lumped network (NL<sub>2</sub>N)-FDTD approach," *IEEE Trans. Microw. Theory Techn.*, vol. 48, no. 12, pp. 2277–2282, Dec. 2000.



**Xue Wu** (S'13) received the B.S. degree in electronic engineering from Tsinghua University, Beijing, China, in 2012, and the M.A. degree from Princeton University, Princeton, NJ, USA, in 2014, where he is currently pursuing the Ph.D. degree in silicon-based terahertz (THz) electromagnetic systems.

His current research interests include exploring techniques for realizing innovative silicon-based integrated systems in the mm-Wave and THz frequency range.

Mr. Wu was a recipient of the National Scholarship of China in 2009, the "Friend of Tsinghua" Scholarship in 2010, and the Academic Scholarship of Tsinghua University in 2011. He was also a recipient of the IEEE Microwave Theory and Techniques Graduate Fellowship and the Analog Devices Outstanding Student Designer Award in 2016.



**Kaushik Sengupta** (M'12) received the B.Tech. and M.Tech. degrees in electronics and electrical communication engineering from IIT Kharagpur, Kharagpur, India, in 2007, and the M.S. and Ph.D. degrees in electrical engineering from the California Institute of Technology, Pasadena, CA, USA, in 2008 and 2012, respectively.

He was a Researcher with the University of Southern California, Los Angeles, CA, USA, and the Massachusetts Institute of Technology, Cambridge, MA, USA, in 2005 and 2006, respectively, where he

was involved in nonlinear integrated systems for high-purity signal generation and low-power RF identification tags. He joined as a Faculty Member with the Department of Electrical Engineering, Princeton University, Princeton, NJ, USA, in 2013. His current research interests include high-frequency ICs, electromagnetics, and optics for various applications in sensing, imaging, and high-speed communication.

Dr. Sengupta was a recipient of the IBM Ph.D. Fellowship from 2011 to 2012, the IEEE Solid State Circuits Society Predoctoral Achievement Award in 2012, the IEEE Microwave Theory and Techniques Graduate Fellowship in 2012, and the Analog Devices Outstanding Student Designer Award in 2011. He was a recipient of the Charles Wilts Prize in 2013 from the Department of Electrical Engineering, Caltech, for Outstanding Independent Research in Electrical Engineering leading to a Ph.D. He was also a recipient of the Prime Minister Gold Medal Award of IIT Kharagpur in 2007, the Caltech Institute Fellowship, the Most Innovative Student Project Award of the Indian National Academy of Engineering in 2007, and the IEEE Microwave Theory and Techniques Undergraduate Fellowship in 2006. He serves on the Technical Program Committee of the European Solid-State Circuits Conference and Custom Integrated Circuits Conference. He was included in the Princeton Engineering Commendation List for Outstanding Teaching in 2014. He is the co-editor of the book *RF and mm-Wave Power Generation in Silicon* (Elsevier, 2015). He was a co-recipient of the IEEE RFIC Symposium Best Student Paper Award in 2012 and the 2015 IEEE MTT-S Microwave Prize.